Journal of Applied Physics ARTICLE pubs.aip.org/aip/jap

Reducing radar cross section of flat metallic targets using checkerboard metasurface: Design, analysis, and realization

Cite as: J. Appl. Phys. **134**, 044902 (2023); doi: 10.1063/5.0154916
Submitted: 17 April 2023 · Accepted: 9 July 2023 ·
Published Online: 24 July 2023

Chao Wang,[1] Ru-Zhi Wang,[1,a)] Sheng-Jun Zhang,[2] Han Wang,[1] and Wen-Song Wang[3]

AFFILIATIONS

[1]Faculty of Materials and Manufacturing, Beijing University of Technology, Beijing 100124, China
[2]Key Laboratory of Experimental Physics and Computational Mathematics, Beijing Aerospace Long March Aircraft Research Institute, Beijing 100076, China
[3]School of Electrical and Electronic Engineering, Nanyang Technological University, Singapore 639798, Singapore

[a)]**Author to whom correspondence should be addressed:** wrz@bjut.edu.cn

ABSTRACT

Aiming at the large-scale application of metasurface in the field of radar stealth, we present a hybrid resonance-based and dispersion substrate integrated checkerboard metasurface (CMS) for reducing the radar cross section (RCS) of flat metallic targets. Considering the frequency-dependent characteristics of such a dispersion material, a pair of single and dual resonant artificial magnetic conductor meta-atoms with the modified "crusades-like" cell topologies is employed to maximize the operating bandwidth; besides, a comprehensive and thorough investigation on the resonance mechanism is conducted in this paper to provide an intuitive physical insight of meta-atoms' reflection responses. By comparing the predicted results with simulations, the quasi-periodic effect is introduced to explain the frequency shift of 10 dB RCS reduction bandwidth. In the implementation procedure, a prototype of the designed RCS reducer with a total dimension of $180 \times 180\ \text{mm}^2$ is fabricated and measured, the 10 dB RCS reduction bandwidth of theoretical simulation and experimental measurement are basically consistent, and the performance improvement of 8 dB RCS reduction in the experimental results can be attributed to the dispersion effects of the dielectric substrate. With a better figure of merit, our efforts may serve as a useful exemplar for the economical CMS architecture in radar evasive applications.

I. INTRODUCTION

The rapid development of intelligent information technology has led to continuous innovation in the radar detection system and prompted the stealth performance of military platforms to receive widespread attention. Generally, the radar cross section (RCS) is used as a quantitative measure to characterize the stealth capabilities of targets against the radar waves. According to the radar range equation,[1] when the RCS of a specified object decreases by an order of magnitude, the maximum detection distance of radar will shrink to $1/\sqrt[4]{10}$ of the original. Conventionally, there are two mainstream strategies for reducing the RCS of targets: coating radar absorbing materials and shape optimization.[2] However, these designs either are bulky or affect the aerodynamic properties of the aircraft, which is defective in practical applications.[3] Fortunately, with the advent of metamaterial and metasurface (MS), the means of regulating electromagnetic (EM) waves have become more flexible and abundant.[4–9] With regard to reducing the RCS for metallic targets by using these novel devices, the methods can be classified into four main types: absorption,[10–13] diffusion,[14] hybrid absorption-diffusion,[15,16] and anomalous reflection.[17,18]

Relying on the anomalous reflection, checkerboard metasurface (CMS) is one type of MS used for RCS reduction that features a short design cycle, easy on-chip fabrication, and many other advantages. In 2007,[19] Paquay *et al.*, for the first time, utilized an artificial magnetic conductor (AMC) in coordination with a perfect electric conductor (PEC) to create a checkerboard-patterned MS for reducing the backscattered EM energy of the targets. Based on the principle of destructive interference, this type of low

backscattering EM modulation device exhibits a high RCS reduction at the resonance frequency; and it does not need to improve performance by compromising the thickness of the structure the way Salisbury screens do.[20,21] Nevertheless, the CMSs constructed by the AMC–PEC combination suffer from narrow RCS reduction bandwidth due to the relatively narrowband characteristics of the early-stage AMC elements. To overcome this drawback, in 2011,[22] an AMC–AMC type of CMS was proposed by Cos *et al.*, which provides a broader bandwidth than a PEC-AMC pair. In the subsequent literature, researchers were committed to stretching the RCS reduction bandwidth by introducing different AMC unit cells.[23–26] According to the previous works, a majority of the early-stage CMSs that are used for RCS reduction have adopted the single resonant AMC structures; however, due to the nonlinear relationship between the operating frequency and the reflection phase, it is difficult to keep the phase curves of the AMC elements parallel to each other in the wideband regime. Therefore, the multiresonant AMCs were applied to broaden the monostatic RCS reduction bandwidth, recent studies deliver evidence that the CMSs assembled by the multiresonant elements in combination with the single resonant elements are better candidates for applications in wideband RCS reduction.[27–30] In addition, following the antenna array theory, a phase difference ranges from 143° to 217° between the elements that enabled the realization of 10 dB RCS reduction has been proposed earlier in 2009.[31] Subsequently, the systematic analysis and validation of the phase deviation requirement of 180° ± 37° for a backward-scattering reduction of 10 dB was carried out by Chen *et al.* in 2015.[24] Since then, the RCS reduction method that combines the conventional phase deviation condition with hybrid CMSs composed of single- and multiple-resonant AMC unit cells has continuously emerged in the literature; and remarkable progress has been achieved.[32–36] According to the analysis of these efforts, when exploiting such a structure to accomplish the low backscattering characteristics of the reflective-type MS, the customary design procedure involves searching for the specified structures with unity reflection amplitude and equidistant phase deviation over the entire operating bandwidth where RCS reduction is to be achieved. However, these design guidelines are often difficult to balance due to the presence of ohmic and tangent losses for the dispersion medium (e.g., FR4). In other words, the fundamental causes of this phenomenon can be explained by the EM parameters of the dielectric substrate that are not only closely related to its own industrial composition (i.e., the resin content or the glass weave style), but are also influenced by the test frequency.

In this paper, we proposed a typical CMS for broadband monostatic RCS reduction; for the sake of generality, the two designed AMC unit cells with single and dual resonant characteristics are constructed using the low-cost FR4 material. Due to the inevitable resonance losses, the reflection amplitudes of the meta-atoms cannot be approximated as 1 in the working band and, therefore, the phase difference of 180° ± 37° is properly adjusted to maximize the bandwidth of 10 dB RCS reduction. The simulation and experimental results validate that the proposed CMS can reduce the backward scattering under normal incidence for 10 dB with a fractional bandwidth (FBW) of ≥ 65.6%. The simulations match well with the measurements in the frequency range of 8–13 GHz, the disagreement observed in the frequency ranges of 13–15.5 and 16–18 GHz, which results in an approximate 77% fractional bandwidth (FBW) for the 8 dB RCS reduction, can be attributed to frequency dispersion of dielectric. In addition, the quadruple symmetrical elements lead to better polarization insensitive properties of the proposed CMS. This paper provides a good reference for future research on the low-cost CMS design.

II. MECHANISM AND CONFIGURATION DESIGN OF THE LOW-RCS CMS

A. Mechanism analysis

In general, for an arbitrary reflective-type MS element illustrated in Fig. 1(a), its response properties to the external EM excitation play a vital role in the field of wavefront modulation. For the natural materials, the permittivity ϵ and permeability μ as intrinsic parameters of the substance can fully describe the dispersion properties of the material, but they cannot intuitively show the structural properties of the MSs in response to the EM waves. Therefore, the artificially synthesized subwavelength textured surfaces are usually equivalent to a layer of EM impedance surface, when the EM wave is coupled to a discontinuous part of the surface, it will lead to the accumulation of polarized charges on the boundary, resulting in an equivalent capacitance, and when the EM wave is coupled to a continuous part of the structure, the surface conductive current flow will continuously flip according to the electric field polarization, thus forming an equivalent inductance. Ultimately, the LC resonant circuit composed of inductor L and capacitor C in series or parallel can clearly demonstrate the resonance relationship between the MS structure and the EM waves. Based on the above analysis, the mechanism model for the interaction between EM waves and MS can be explained through a semi-infinite length transmission line (TL),[37] as shown in Fig. 1(b).

In this model, a section of TL with distance R and intrinsic impedance $Z_0 = 377\ \Omega$ represents the free space.[38] The other section of TL with short circuit at the end represents the metal-backed dielectric spacer of the MS; notably, for the dispersion medium

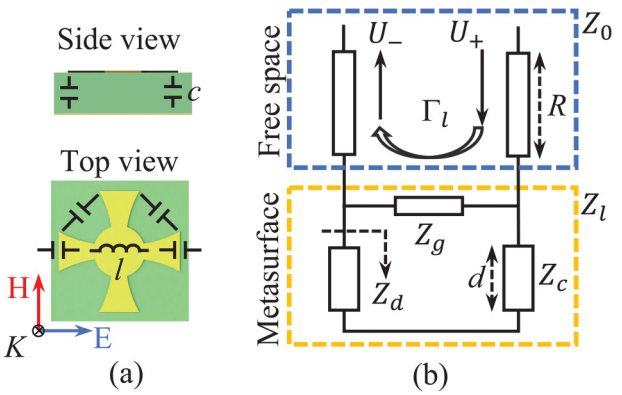

FIG. 1. (a) Schematic diagrams of the reflective-type MS element, yellow color indicates the metal, and green color indicates the dielectric substrate. (b) The mechanism model for the interaction between EM waves and MS.

(e.g., FR4), the characteristic impedance, Z_c, of this piece of TL with a length of d is usually frequency-dependent. The impedance Z_g connected in parallel between the two TLs symbolizes the top layer metal patch. Z_d is the impedance by the shorted TL, which is expressed as $Z_d = -jZ_C \tan \beta d$, where β is the phase constant of the incident wave. If the MS of this sandwich structure is considered a whole, the complex impedance of the termination load in the TL model can be expressed by $Z_l = R_l + jX_l$ and $Z_l = Z_g \parallel Z_d$. According to the TL theory, the reflection coefficient Γ_l at the terminal, which represents the mismatch between Z_0 and Z_l, can be obtained by the following equation:[37]

$$\Gamma_l = \frac{Z_l - Z_0}{Z_l + Z_0} = \frac{R_l^2 - Z_0^2 + X_l^2}{(R_l + Z_0)^2 + X_l^2} \pm j\frac{2X_l Z_0}{(R_l + Z_0)^2 + X_l^2} \quad (1)$$

Using amplitude-phase representation, the reflection coefficient can be abbreviated as $\Gamma_l = |\Gamma_l| e^{\pm j\varphi_l}$, where the reflection amplitude and phase are calculated by[39]

$$|\Gamma_l| = \sqrt{\frac{(R_l - Z_0)^2 + X_l^2}{(R_l + Z_0)^2 + X_l^2}}, \quad (2)$$

$$\varphi_l = \arctan\left(\frac{2X_l Z_0}{R_l^2 + X_l^2 - Z_0^2}\right). \quad (3)$$

After getting these two key regulatory factors, the principle of employing CMS to reduce the backscattering energy is that the scattered field will cancel and generate different scattering patterns when the specified reflection phases are arranged in a checkerboard grid. The physical mechanism behind this destructive interference behavior between the reflected EM waves can be explained by the antenna array theory. Considering a 2D planar array of MS with M × N meta-atoms under normal incidence, the scattering field $E^s(\theta, \varphi)$ can be expressed as the product of element pattern $f(\theta, \varphi)$ and array factor AF (θ, φ) where θ and φ are the elevation and azimuth angles of the reflected waves. In most cases, the beamwidth of element pattern is wide enough; therefore, we can get the radiation properties of the MS array directly by investigating the array factor and neglecting the influence of the element pattern when the number of elements is large. As for the array factor, the common representation is defined as[1]

$$AF(\theta, \varphi) = \sum_{m=1}^{M}\sum_{n=1}^{N} A_{m,n} e^{j[k_0 \sin\theta(\cos\varphi \cdot md_x + \sin\varphi \cdot nd_y) + \varphi_{m,n}]}, \quad (4)$$

where $A_{m,n}$ and $\varphi_{m,n}$ are the reflection amplitude and phase of the (m, n)th element in the array, respectively. k_0 denotes the wavenumber vector. d_x and d_y are the spacing between the elements along x- and y-directions. For an arbitrary binary MS under normal incidence, the array factor in the backward direction ($\theta = 0°$) can be simplified as

$$AF(\theta, \varphi)|_{(\theta=0°)} \sum_{m=1}^{M}\sum_{n=1}^{N} A_{m,n} e^{j\varphi_{m,n}}. \quad (5)$$

Specially, when the MS is specified as a CMS with an equal number of elements "0" and "1," the reflection coefficient of the entire surface can be approximated by the average value of the two types of elements; therefore, the array factor can be further reduced to the following equation:

$$AF(\theta, \varphi)|_{(\theta=0°)} = \frac{A_{r0} \cdot e^{j\varphi_{r0}} + A_{r1} \cdot e^{j\varphi_{r1}}}{2}, \quad (6)$$

where A_r and φ_r are the reflection amplitude and phase of both elements.

The monostatic RCS reduction of the MS compared to an equal-sized metal plate is defined by

$$\sigma_{r(MS)} = 10 \log\left[\frac{|E^s|^2}{|E^i|^2}\right], \quad (7)$$

where E^i is the incident electric field, which is usually normalized to 1 and E^s represents the scattered electric field. Combining the above two equations, the RCS reduction of CMS can be approximated by[24]

$$\sigma_{r(CMS)} = 10 \log\left[\frac{A_{r0} \cdot e^{j\varphi_{r0}} + A_{r1} \cdot e^{j\varphi_{r1}}}{2}\right]^2, \quad (8)$$

where the reflection amplitudes A_{r0} and A_{r1} are usually unity in most designs that employ a dielectric material with relatively low loss as the supporting substrate; therefore, to achieve the RCS reduction of 10 dB or more, the phase deviation between the two elements is required to be maintained within the 143°–217° range.[29] In addition, it is worth emphasizing that Eq. (8) can provide an efficient method to quickly predict the performance of RCS reduction for the designed CMS, by neglecting the mutual coupling between the adjacent elements and edge effects. However, this guideline for RCS reduction fast estimation is obtained on the basis of certain simplifications and approximations (e.g., $A_{r0} \approx A_{r1} \approx 1$), which is not particularly applicable in the low-cost lossy FR4 substrate applied in our work. That is to say, the phase deviation for theoretically predicting the frequency range of 10 dB RCS reduction needs to be modified appropriately to cater the increased bandwidth due to the substrate loss.[17,40] In the following, two different AMC elements with single and dual resonance are designed to achieve the phase deviation criterion that satisfies the 10 dB RCS reduction over a wide frequency range.

B. Configuration design of the low-RCS CMS

The typical CMS is one type of MS consisting of two kinds of counter-phase elements arranged in a chessboard-like manner. The structure of the elements is usually composed of three parts: the top layer metal patch, the middle layer dielectric spacer, and the bottom metallic backplate. As an essential component of a

reflective-type MS structure, the metallic backplate tends to be constructed with a thin layer of copper, which means that it does not require excessive attention during the design process. The intermediate dielectric interlayer and the top metal patch are the key aspects that need to be considered. In the previous theoretical analysis, the EM parameters and thickness of the dielectric substrate determine the value of impedance Z_d, and the shape and size of the metal patch determine the value of impedance Z_g, by connecting the two impedances in parallel, the input impedance of the MS (i.e., the load impedance Z_l), which is closely related to the reflection coefficient, can be obtained. In some designs with low-loss dielectric substrates, Z_d can be obtained directly by means of analytical calculations.[41] However, it is difficult to summarize a generalized equation for solving Z_g due to the ever-changing geometries of the metal patches according to different design purposes. Moreover, the frequency-dependent characteristics of the dispersion mediums will also cause the theoretical calculations to deviate from the actual values. Consequently, the method of reverse acquisition for structure parameters based on expected S-parameters and analytic equations is often difficult, especially in some designs with low-cost and lossy FR4 substrate.

In this paper, the configuration design of the two adopted AMC elements is carried out by a "forward enumeration" method, i.e., the parametric sweep function of CST Microwave Studio, which enables a convenient and efficient execution of several simulations with different structure parameter values. Before performing such an operation on the structure of the meta-atom, a basic element of MS should be predefined. Inspired by the crusades-like pattern,[42] Fig. 2(a) gives the 3D structure of the original element to be optimized, the periodical dimension (p) of which is 7.5 mm, and the thickness of the dielectric spacer (t) is 3 mm. The metallic pattern and backplate are copper with a thickness of 0.036 mm and conductivity of 5.8×10^7 S/m.[43] The employed dielectric substrate is FR4 material with a relative permittivity of 4.3 and a loss tangent of 0.025. The variable dimensional parameters are w_1, w_2, w_3, l_1, and l_2, respectively. In the simulation, the periodic boundary conditions are assigned to the lateral walls of the element; and the Floquet port is placed at 10 mm distance (about 0.36 λ at 11 GHz) from the top surface of the structure to extract the reflection coefficients of meta-atoms under the vertical illumination of a plane EM wave. Noteworthily, for normal incidence, two types of linear polarizations can be excited; however, the fourfold symmetrical meta-atom makes these excitations essentially identical. Therefore, only the electric field along the x-direction (corresponding to the TM00 mode) was considered during the geometry optimization of the metal patches. Figures 2(b) and 2(c) present, respectively, the reflection amplitudes and phases of the initial meta-atoms with variable dimensional parameters

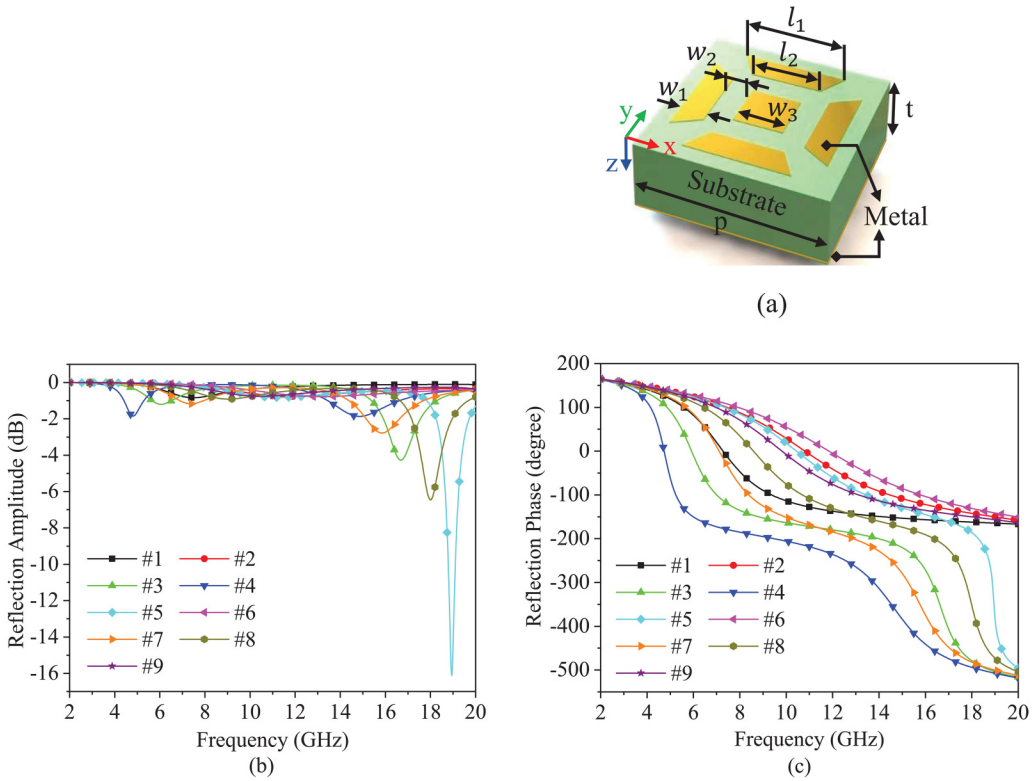

FIG. 2. (a) Schematic of the original element to be optimized. [(b) and (c)] The reflection amplitudes and phases of the initial element with different geometry parameters.

TABLE I. Variable dimensional parameters in millimeters.

Parameter	w1	w2	w3	l1	l2
No. 1	2.0	0.5	2.7	5.5	2.7
No. 2	0.5	0.5	2.5	2.0	2.5
No. 3	1.0	0.5	2.5	7.0	2.5
No. 4	0.5	1.5	2.5	7.0	2.5
No. 5	0.5	0.5	1.0	3.0	1.0
No. 6	0.5	1.5	1.0	1.0	1.0
No. 7	1.0	0.5	2.0	5.0	2.0
No. 8	2.5	0.5	1.5	1.0	1.5
No. 9	1.5	0.5	1.5	4.0	1.5

enumerated in Table I. It is observed that elements 1, 2, 6, and 9 feature single resonance, while elements 3, 4, 5, 7, and 8 exhibit a dual resonant behavior. Furthermore, the inverse increased resonance peaks, as shown in Fig. 2(b), will contribute to the expansion of RCS reduction bandwidth. From Fig. 2(c), it is also found that the decrement in patch area or spacing can provide a blue-shift in the reflection phase response. Meanwhile, for these dual resonant elements, the quality factor (Q) at the resonant frequencies exhibits, respectively, a decreasing and increasing trend in the frequency range of 2–11 and 11–20 GHz, as the patch geometry varies. Where element 5 with the minimum patch area and maximum patch interval experienced a sharp decrease in the phase response from 18 to 20 GHz due to its higher Q value. Since this high Q value and rapid phase-decreasing phenomenon will reduce the bandwidth of RCS reduction, therefore, to achieve the wideband performance of scattering reduction, the optimal metallic pattern pair should be equipped with different low Q values.[3]

According to the abovementioned analysis, and under the premise of ensuring the phase deviation of 180° ± 37° for 10 dB RCS reduction covers a wider frequency range, the elements with in-phase and out-of-phase reflections around the center frequency of 11 GHz (i.e., no. 2, no. 7) are selected to construct the proposed CMS in this paper. The comprehensive comparison of the reflection coefficients and Q values between the two AMC elements can be found in our previous work.[44] Based on the results, it can be inferred that the phase deviation between these two AMC meta-atoms is well maintained around the angular range of 143°–217° from 7.6 to 15.5 GHz. The slight phase deteriorations of this phase deviation criteria (180° ± 37°) are neglected due to the substrate loss. Additionally, it is noted that the simulated cross-polarization reflection coefficients of the chosen elements are both lower than −50 dB under the normal incidence of TM wave; therefore, only the co-polarization reflection coefficients are concerned in this paper.

Figure 3(a) illustrates the construction of the checkerboard combination from the two types of elements, which consists of 6 × 6 AMC group cells, and each group cell contains 4 × 4 meta-atoms. The overall dimensions of the designed CMS are 180 × 180 mm^2. Here, it is worth mentioning that, under normal incidence, the number of meta-atoms comprising one AMC group cell does not affect the RCS reduction performance of the

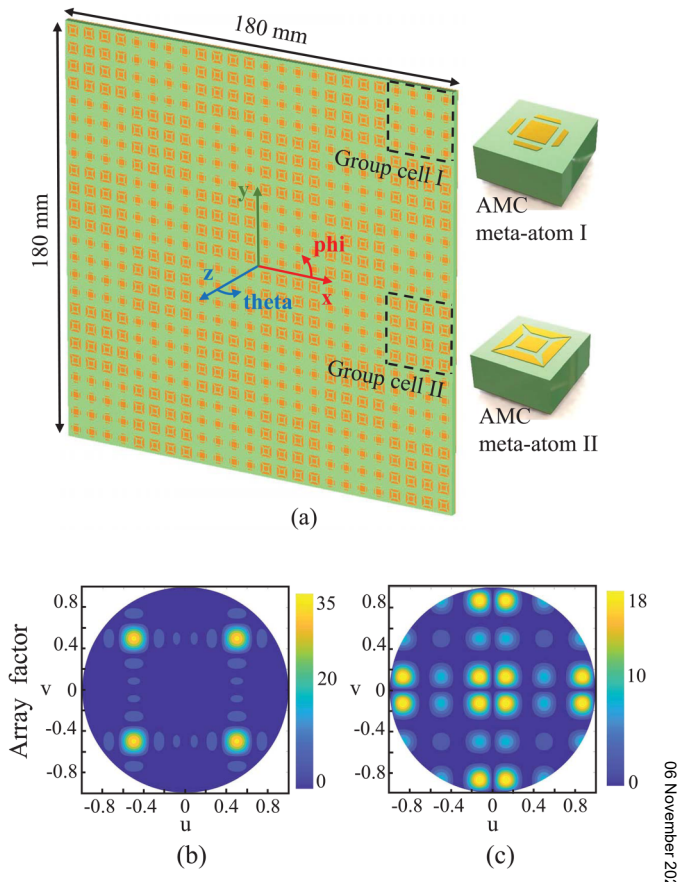

FIG. 3. (a) 3D configuration of the proposed CMS. (b) Array factor of CMS with group cell composed of 4 × 4 meta-atoms. (c) Array factor of CMS with group cell composed of 12 × 12 meta-atoms.

proposed CMS along the z-direction. However, it determines the elevation and azimuth angles of the maximal scattering fields in the backward direction, which can be calculated by the generalized Snell's law or the antenna array theory.[1] Specifically, analysis from the anomalous reflection, we assume that the phase difference of 180° between the two meta-atoms was obtained at a certain frequency (e.g., 10 GHz), combining Eq. (11), it is known that the position of the four scattered mainlobes can be controlled by the dimension of the AMC group cell. In this paper, the designed elevation angles of the four mainlobes are 45°; therefore, the dimension of the group cell is 30 × 30 mm^2. Under the same assumptions, the calculated array factors of equal-sized CMSs with group cell composed of 4 × 4 and 12 × 12 meta-atoms are given in Figs. 3(b) and 3(c), as it can be seen, the reflected mainlobes will gradually approach the normal position with the increase in AMC group cell dimension. Such evidence proves that the group cells containing 4 × 4 meta-atoms have better performance for reducing the monostatic and bistatic RCS of flat metallic targets.

III. SIMULATION AND ANALYSIS

A. Physical interpretation and analysis of meta-atoms' reflection characteristics

To understand more intuitively about the physical mechanism behind the reflection characteristics of the two AMC meta-atoms, the elements' reflection coefficients have been examined in this part from various perspectives.

First, the normalized Smith Chart is introduced to further demonstrate the meta-atoms' reflection characteristics, as shown in Figs. 4(a) and 4(b), it is obvious that meta-atom I features only one magnetic resonance at 10.8 GHz, while meta-atom II exhibits, respectively, two magnetic resonance points and one electric resonance point at 7.1, 15.8, and 11.6 GHz. The in-phase (or out-of-phase) reflections correspond to the resonant points of the meta-atoms, beyond which the surface impedance becomes capacitive (or inductive). Furthermore, for these magnetic resonances, the real part of the equivalent surface impedance reaches a maximal as the imaginary part approaches zero, indicating that the proposed meta-atom has the properties of a perfect magnetic conductor; similarly, for the electric resonance, both the real and imaginary parts of the equivalent surface impedance are simultaneously close to zero, meaning that the meta-atom acts as an electric dipole. The magnitude of real part of the corresponding impedance at magnetic resonance points determines the extent of dip in reflection amplitudes, in other words, the gradually decreased real part of equivalent surface impedance results in Z_l becoming closer to Z_0, which enables more EM energy to penetrate the meta-atom and leads to an increased dielectric loss. The approximately 0.3 dB of return loss of meta-atom II at the electric resonance point (11.6 GHz) is originated from the ohmic loss of the FR4 material.

The subsequent investigations focus on the current distribution of meta-atom II due to its presence of both magnetic resonance and electric resonance. Figures 5(a)–5(c) depict the surface current distribution of meta-atom II under the normal incidence of y-polarization at the three resonant points mentioned above; additionally, the phase distributions of H-field's x-component under different profiles are also plotted in the figure to give a more complete physical comprehension. From Figs. 5(a) and 5(c), it is manifested that the surface current flows in the opposite directions on the top and bottom metallic components of the meta-atom, and these anti-parallel currents can build a looped field around the incident magnetic field, thus creating a strong magnetic resonance. This effect produces a surge in the magnetic permeability and leads to a higher equivalent surface impedance of the meta-atom compared to the impedance of free space, thus making the meta-atom performs as a high impedance surface with zero reflection phase at the resonant points of 7.1 and 15.8 GHz. Correspondingly, the phase distribution of the x-component of the induced magnetic field in XY (at $Z = -3.035$) and YZ (at $X = 0$) planes reveals that the direction and magnitude of the magnetic field in the dielectric substrate are basically the same; therefore, by applying the boundary conditions of tangential magnetic field on the metallic surface, it can be inferred that the currents on the bottom metallic backplate will also be uniformly distributed when magnetic resonance occurs. The main difference between the two types of magnetic resonance lies in the current distribution on the top layer metal patch. As can be seen from Figs. 5(a) and 5(c), the current originally located at the peripheral trapezoidal structures of the patch is switched to the central square metal sheet when the resonant frequency rises from 7.1 to 15.8 GHz. This phenomenon reduces the resistance of the current flow on the patch due to which the equivalent surface impedance of the meta-atom decreases from 15 (at 7.1 GHz) to 6.4 (at 15.8 GHz). Comparing the current distribution diagrams of electric resonance and the two types of magnetic resonance, as shown in Fig. 5, it is found that

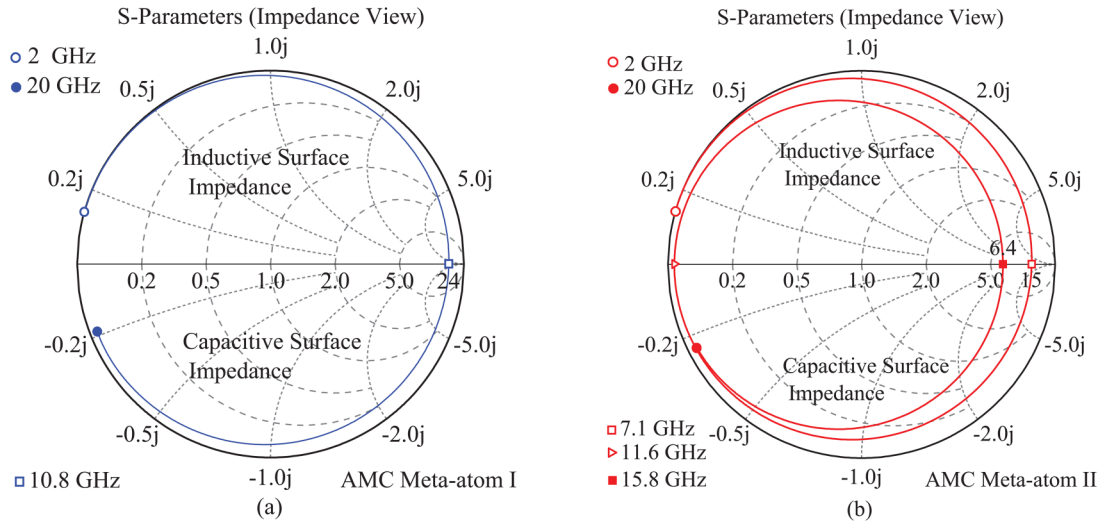

FIG. 4. Reflection coefficient of the AMC elements in Smith Chart. (a) AMC meta-atom I. (b) AMC meta-atom II.

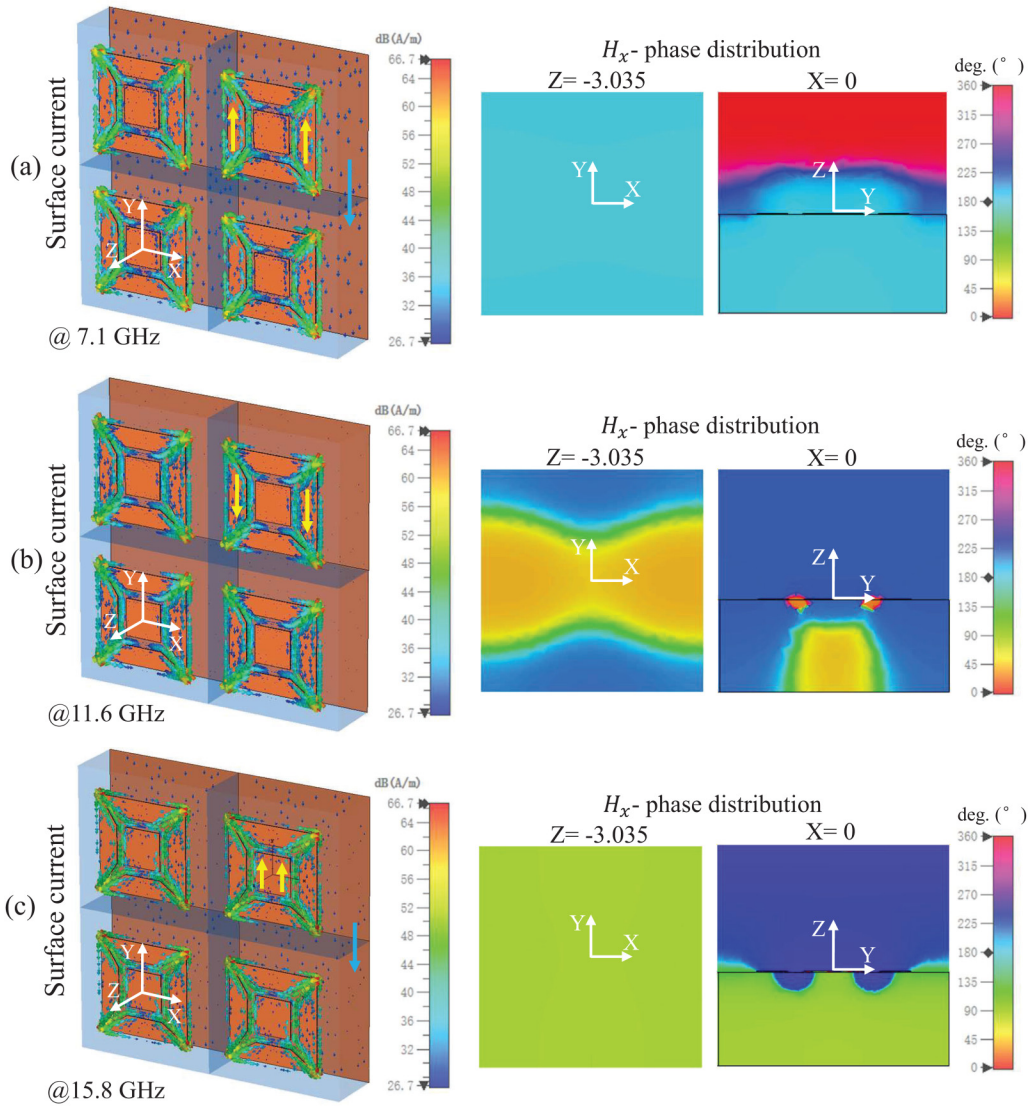

FIG. 5. Distribution diagrams of surface current and phase of the induced H-field's x-component of meta-atom II under the normal incidence of y-polarization. (a) At 7.1 GHz. (b) At 11.6 GHz. (c) At 15.8 GHz. The yellow and blue arrows represent the directions of the current flow on the top metal patch and bottom metallic backplate, respectively.

when electric resonance occurs, the currents distributed on the bottom metallic backplate become feeble due to the nearly out-of-phase magnetic field distribution in the dielectric spacer. The parallel current distributions on top and bottom metal parts capable of producing electric dipole resonances do exist; however, they are not apparent. Considered from another point of view, the incident EM waves can be reflected directly into the free space after impinging on the top metal patch, and thereby the losses in the middle layer dielectric spacer can be ignored during the electric resonance at 11.6 GHz.

Following the foregoing discussion, we also explored the magnitude and phase distributions of the E-field's components at a distance of 0.01 mm from the surface of meta-atom II at 7.1 and 15.8 GHz, as illustrated in Fig. 6. It is clearly shown that the magnitude of E_x-components (i.e., the cross-polarized components) at both resonant frequencies is significantly reduced in the principal planes due to the out of phase cancellation property of the meta-atom itself. The normal components, E_z, are shorted out on the bottom metallic backplate. Furthermore, the changes in the distribution of E_y-components (i.e., the co-polarized components) at

the two resonant points indicate that the source of the EM coupling is transformed from the outside of the metal patch to its inner region, which exactly corresponds to the variation of current distributions demonstrated in Figs. 5(a) and 5(c). The weakened mutual coupling between the adjacent elements as shown in Fig. 6(e) can be attributed to the element spacing (2.5 mm) being larger than 0.25 wavelengths in the dielectric (2.3 mm).[45]

In the end, we plotted the power loss of the meta-atom at the two magnetic resonance points as shown in Figs. 7(a) and 7(b). It is obvious that the changes in the distribution of energy loss are consistent with those of the E_y-components plotted in Figs. 6(b) and 6(e), the losses at 7.1 and 15.8 GHz are mainly originated from the dielectric loss of FR4.

B. RCS reduction performance analysis of the proposed CMS

The transmission line matrix (TLM) based time-domain (TD) solver of CST software is adopted to evaluate the RCS reduction performance of the proposed CMS. In the simulation setup, the

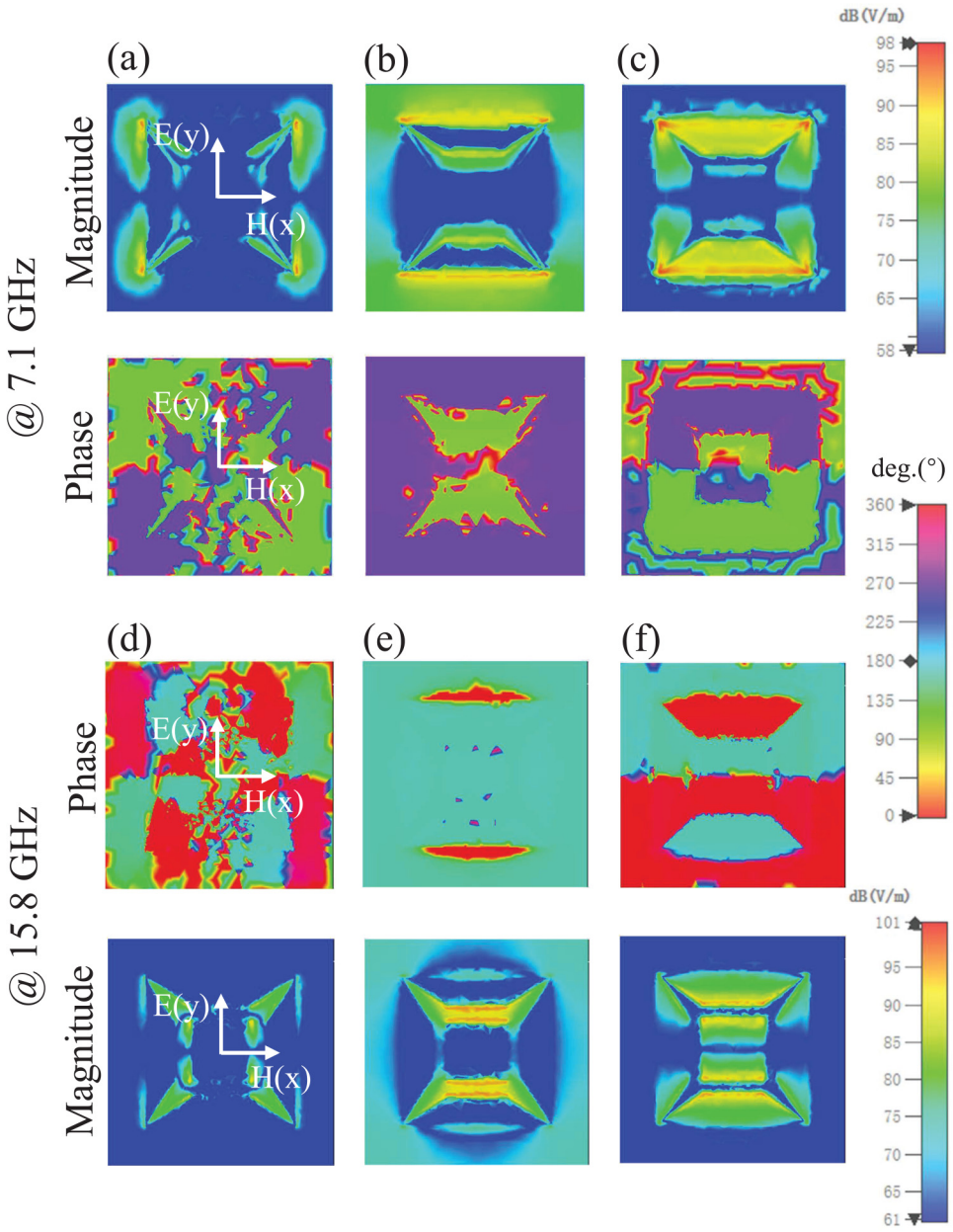

FIG. 6. The magnitude and phase distributions of the E-field's components at a distance of 0.01 mm from the surface of meta-atom II at 7.1 and 15.8 GHz. [(a) and (d)] E_x-component. [(b) and (e)] E_y-component. [(c) and (f)] E_z-component.

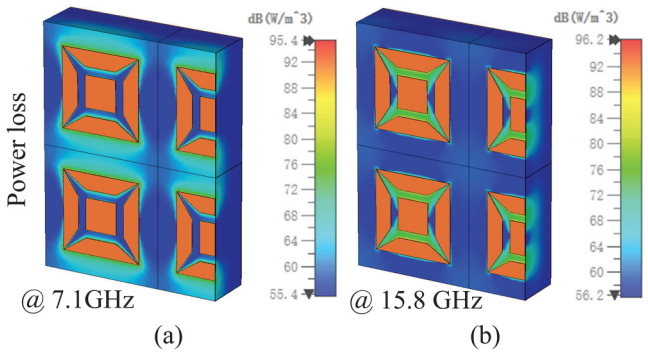

FIG. 7. The power loss distributions of meta-atom II at the two magnetic resonance points. (a) 7.1 GHz. (b) 15.8 GHz.

"open add space" boundary condition is loaded on all sides of the metasurface; besides, to improve the accuracy of the simulation, a local mesh refinement is applied on the top layer metal patch. Figure 8 depicts the simulated monostatic RCS curves of the designed CMS and the reference PEC surface for TM polarized wave normal incidence. It is observed that the co-polarized RCS curve of the CMS features two valleys located at 8.56 and 11.15 GHz, respectively, and the cross-polarized result with the maximum value below −24 dBsm throughout the whole bandwidth can be neglected in comparison with the reference PEC surface.

The simulated monostatic RCS reduction for normal-incidence excitations is compared with the predicted results based on Eq. (8), as shown in Fig. 9. Data from the simulation show that the proposed CMS is capable of achieving more than 10 dB RCS reduction over the frequency range of 8.1–16 GHz,

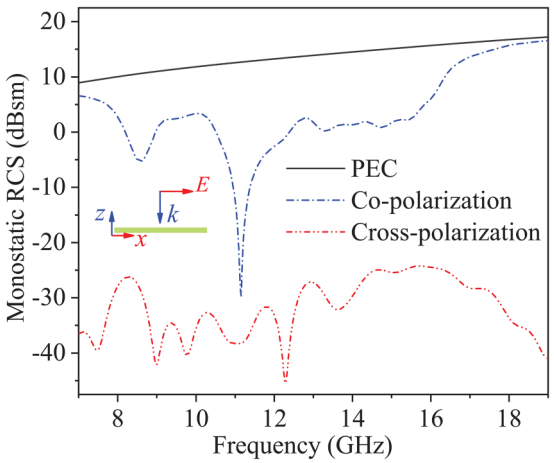

FIG. 8. The simulated monostatic RCS results of the designed CMS and the reference PEC surface for TM polarized wave normal incidence.

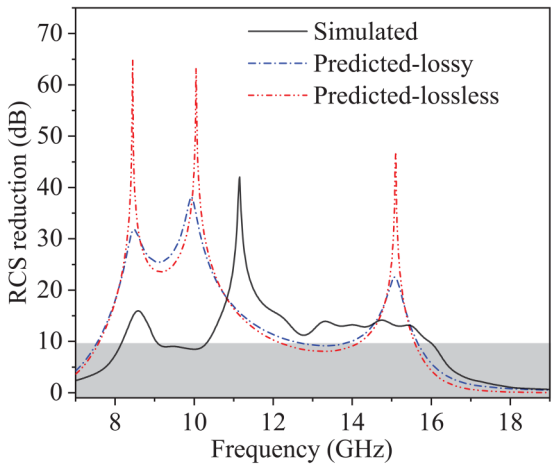

FIG. 9. The simulated and predicted backward-scattering RCS reduction for the designed CMS under normal-incidence excitations.

which exhibits a trend of rightward movement from the frequency range of conventional phase deviation criteria for 10 dB RCS reduction (7.6 to 15.5 GHz); this phenomenon can be ascribed to the fact that the full-wave simulation based on TD solver considered the real mutual coupling, and actual reflection amplitudes of the meta-atoms rather than assuming them to be identical and equal to 1. The peak locations of RCS reduction in the two predicted curves are basically consistent, indicating that the destructive interference between the reflected EM waves is the main reason for the generation of RCS reduction. The swing of meta-atoms' reflection amplitudes from −2.73 to −0.13 dB (Fig. 2) due to the substrate loss can be detrimental to this mutually canceling effect, which, however, enables the prediction to better approximate the simulation. The frequency shift of the maximum peak value of RCS reduction between simulation and prediction is caused by the periodic assumption in the simulation of reflection phase that does not take into consideration the exact surroundings of the meta-atom in a real quasi-periodic array (i.e., the designed CMS),[46] thus leading the designed phase difference between meta-atom I and II to deviate from the practical one.

The bistatic 3D scattering patterns between the proposed CMS and the equal-sized PEC surface under normal incidence are compared in Fig. 10 at 8.56 and 11.15 GHz, respectively. It is observed that the backward scattering of the CMS is much lower than that of the equal-sized PEC surface. The RCS reduction occurs because the single mainlobe originally reflected by the metal plate is redirected into four mainlobes after the reflection by the designed CMS. The elevation and azimuth angles of these mainlobes with equal magnitude can be calculated using the following equations:[44]

$$\theta = \arcsin \frac{\sqrt{(\nabla \Phi_x)^2 + (\nabla \Phi_y)^2}}{\beta_0}, \tag{9}$$

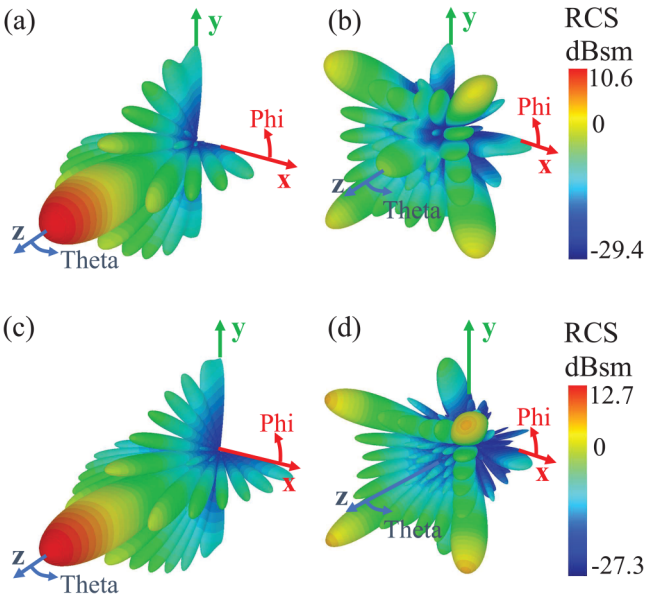

FIG. 10. Comparison of the bistatic 3D scattering patterns between the proposed CMS and the same dimension of PEC surface under normal incidence at different frequencies. [(a) and (c)] For PEC surface at 8.56 and 11.15 GHz. [(b) and (d)] For the proposed CMS at 8.56 and 11.15 GHz.

$$\varphi = \arctan\frac{\nabla\Phi_y}{\nabla\Phi_x}, \tag{10}$$

where $\nabla\Phi_x$ and $\nabla\Phi_y$ are the 2D phase gradients along the x- and y-directions, $\beta_0 = 2\pi f/c$ represents the phase constant in free space, and f is the operational frequency. For CMSs in this paper, we have $\nabla\Phi_x = \nabla\Phi_y = \Phi_{diff}/L$, where Φ_{diff} is the phase difference between the two AMC elements and L represents the physical distance of the AMC group cells. Thus, the above two equations can be simplified as

$$\theta = \arcsin\left|\frac{\sqrt{2}\,\Phi_{diff}}{360\,L/\lambda_0}\right|, \tag{11}$$

$$\varphi = 45^\circ, 135^\circ, 225^\circ, 315^\circ\ . \tag{12}$$

Corresponding to the 3D scattering pattern of CMS at 11.15 GHz [Fig. 10(d)], Fig. 11(a) gives its 2D results based on TD-solver for a more intuitive presentation of the angular information of the RCS pattern. The four scattered mainlobes are observed at $\varphi = 45^\circ, 135^\circ, 225^\circ, 315^\circ$, which are completely consistent with the theoretical calculations, their angles of elevation are all 38°. In addition, using the analytical expression (11), the predicted relationship curve between theta value (θ) and the electrical length of L is plotted in Fig. 11(b). Here, it is worth noting that the Φ_{diff} is obtained based on Floquet's theorem, which automatically considers the mutual coupling between meta-atoms with periodical boundary conditions. Combining Fig. 10 and the analytical curve, it can be inferred that the four mainlobes become narrower and are close to the normal direction as the electrical length of AMC group cell increases. The 45° elevation radiation not only appears at the maximum RCS reduction position of $L = \lambda_0$, but also can be generated at the other value of L/λ_0 as marked in the curve. The angle error of 4 degrees between the TD simulation and the analytical prediction at $L/\lambda_0 = 1.115$ can be attributed to the change of Φ_{diff} due to the quasi-periodic effect.

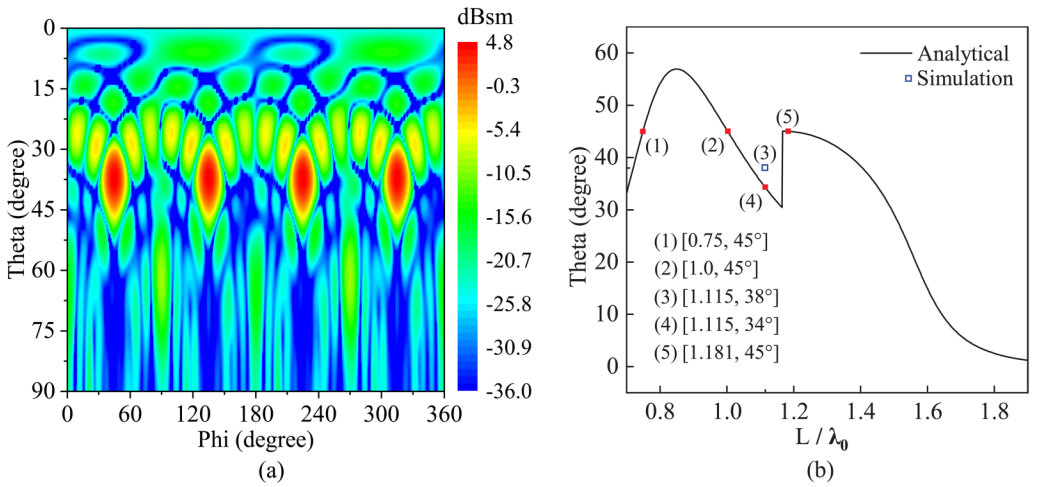

FIG. 11. (a) The bistatic 2D RCS pattern of the proposed CMS under normal incidence at 11.15 GHz. (b) The predicted relationship curve between theta value and the electrical length of the AMC group cell.

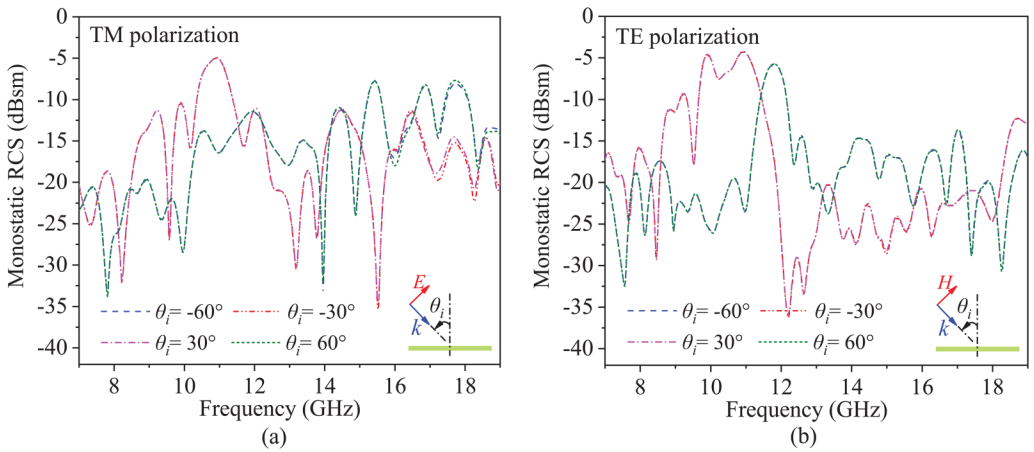

FIG. 12. The simulated monostatic RCS of the designed CMS under oblique incidences for (a) TM and (b) TE polarizations.

The simulated monostatic RCS of the designed CMS under oblique incidences for TM and TE polarizations are provided in Fig. 12. The result curves of $\theta_i = \pm 30°$ (or ±60°) match perfectly, as expected. For oblique incidences, both the wave impedance of free space and surface impedance of the CMS vary with the angle of incidence, and the formulas that describe their changing correlations are distinct depending on the polarization mode. As a result, the reflection phase of meta-atoms as well as the RCS of the proposed MS will no longer maintain the consistent results like the different polarized normal incidences. In addition, the monostatic RCS results are constantly below −10 dBsm except for the frequency range of 10.3–11.3 GHz in TM mode and 9.6–12.1 GHz in TE mode, indicating that more than 90% of the incident EM energy are scattered to the free space in the form of 0th-order and 1st-order reflections. The maximum monostatic radar range of the CMS with oblique incidence is shrunk to less than 0.37 times compared to the PEC surface with normal incidence from 7 to 19 GHz.

Figure 13 shows the simulated mirror bistatic RCS reduction of the proposed CMS under the TM- and TE-polarized oblique incidences. When the incident angle $\theta_i = 15°$, the bandwidths of 10 dB RCS reduction for both TM and TE polarizations are slightly shrunk from that of the normal incidence. For the TM polarization, as the angle of incidence is increased, the RCS reduction performance deteriorates gradually at the higher frequencies, while remaining stable in the x band for the incident angles up to 45°. For the TE polarization, the performance of RCS reduction

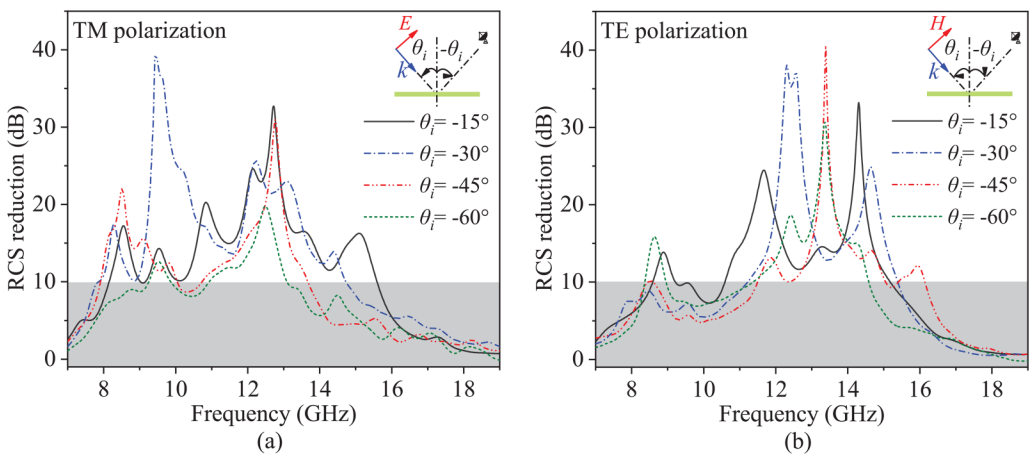

FIG. 13. Bistatic RCS reduction of the proposed CMS under the (a) TM- and (b) TE-polarized oblique incidences.

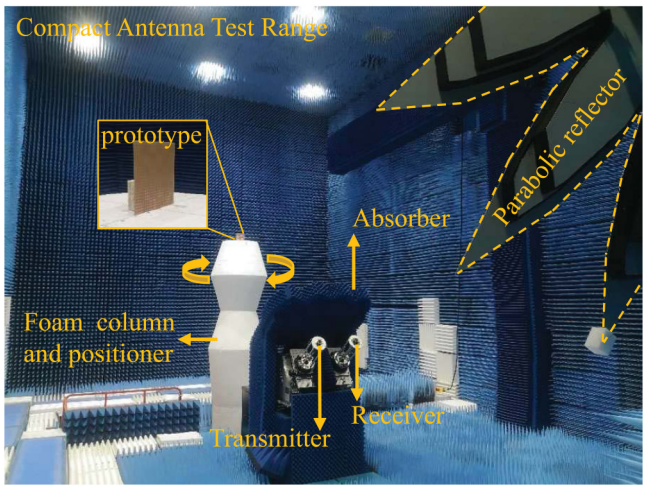

FIG. 14. The photograph of the fabricated prototype and the measurement setup.

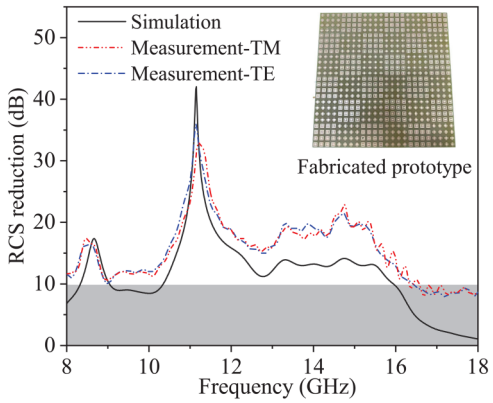

FIG. 15. The RCS reduction performance comparison of the simulated and measured results.

presents a diametrically opposite situation from that of the TM case. In other words, the sum of the space phase delay and the phase difference between the two AMC elements under oblique incidence are more likely to deviate from the phase deviation criteria of 10 dB RCS reduction at higher frequencies for the TM polarization and at lower frequencies for the TE polarization.

IV. EXPERIMENT VERIFICATION

To validate the simulated performance of the proposed CMS, a planar prototype of the designed model was fabricated and measured. The sample was manufactured using the printed circuit board technology, and the measurements were collected in the compact antenna test range system. The photograph of the fabricated prototype and the measurement setup is depicted in Fig. 14. In the picture, the white foam column with extremely low backward scattering can provide good support for the target to be tested. The transmitter and receiver horn antennas operating from 8 to 18 GHz are connected to the two ports of a Rohde & Schwarz-ZVA40 vector network analyzer. The sophisticated parabolic reflector can transform the spherical waves from the transmitter into standard plane waves at a close range.

After undergoing operations such as background subtraction and time-domain gating configuration, the measured RCS reduction was obtained and compared with the simulated results as shown in Fig. 15. As it can be seen, the measurement curves of different polarizations match each other, indicating that the designed CMS has good property of polarization insensitivity to the normally incident. Besides, the bandwidth of 10 dB RCS reduction obtained from the experimental test completely covers that of the computational simulation. In the frequency range from 8 to 13 GHz, a good agreement between simulations and measurements is noted; however, a certain mismatch between the two types of RCS reduction curves in the frequency range of 13–15.5 and 16–18 GHz is also observed. These divergences can be mainly induced by the following two factors: First, the curves of relative permittivity and loss tangent vs frequency used in the simulation were obtained using the fitting algorithm based on the pole-zero dispersion model in CST software, which may exhibit slight deviations from the actual value in the two frequency bands mentioned above, due to the frequency dispersive nature of the real dielectric material. Second, the errors generated from the manufacturing process of the CMS (e.g., metal etching or substrate surface irregularities) can also cause the measurements to deviate from the simulations. However, combining Fig. 18 with the well-matched results as depictured in Fig. 15 (8–13 GHz), we can basically rule out the latter possibility. Therefore, Fig. 16 has been carried out from the perspective of dispersion to give a more tangible understanding about the causes of the deviation between simulations and measurements. Figures 16(a) and 16(b) presents, respectively, the simulated results of RCS reduction and phase difference (Φ_{diff}), with varying relative permittivity ε_r. Based on the TD simulation, Fig. 16(a) provides an intuitive comparison of the simulated RCS reduction curves for the designed CMS under different relative permittivity. As it can be seen, with the relative permittivity decreases from 4.3 to 3.1, the 10 dB RCS reduction bandwidth increases from 13–16 GHz to 13–17.7 GHz, when $\varepsilon_r = 3.7$, the bandwidth of mismatch between the two types of datasets (i.e., the simulated and the experimental data) shrinks from 13–18 GHz with $\varepsilon_r = 4.3$ (in Fig. 15) to 17–18 GHz. On the basis of frequency-domain (FD) simulation, and analysis from the underlying mechanism of the destructive interference, the bandwidth of phase deviation condition ($180° \pm 37°$), as shown in Fig. 16(b), follows the same increasing trend with the decrease in relative permittivity.

To further support the above analysis and verify the reliability of the data, the measured monostatic RCS of the CMS under the oblique incidence corresponding to Fig. 12 is shown in Fig. 17. It is worth mentioning that the measured RCS curves for both TM and TE polarizations at the oblique incident angles of (θ, $\varphi = 0°$) and (θ, $\varphi = 180°$) are no longer exhibiting the consistent behaviors as observed in the simulations. This phenomenon can be explained

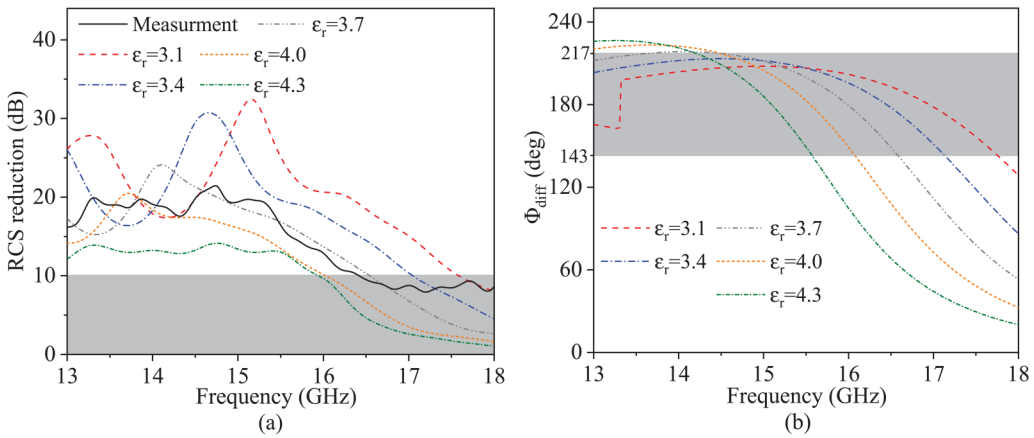

FIG. 16. The simulated curves with varying relative permittivity. (a) The RCS reduction of the designed CMS. (b) Phase difference between the two meta-atoms.

from the two aspects of internal and external factors, in terms of the internal factors, the dielectric constant that exists in the real FR4 substrate is usually in the form of a tensor matrix; therefore, the EM parameters observed from different angles are naturally different, regarding the external causes, in addition to the processing errors, the misalignment between the antenna and the target to be measured can also be a major contributor to this issue.

After comparing the simulated and measured monostatic RCS curves for different incident angles at oblique incidence, it is found that the two kinds of results are consistent well over the entire frequency band from 8 to 18 GHz. Figure 18 shows the comparison diagram of the measurements and the simulations for the incident angles of ($\theta = 60°$, $\varphi = 0°$) at the TE case. The good agreement between the measured and simulated results in the figure provides strong evidence for the accuracy of the simulation method. Additionally, the overshoot and slight frequency shift can be attributed to the effect of the mutual coupling and dielectric properties of the substrate.

At the end of this paper, a comparison between the proposed CMS and the other wideband checkerboard designs is performed and presented in Table II to evaluate its RCS reduction performance under the normal incidence.[47–51] As is known, by conducting a specific numerical calculation on the upper (f_H) and lower (f_L) limit of the operating frequency, the absolute bandwidth or FBW is suited to quantitatively characterize the RCS reduction performance of these devices. However, in some space-borne applications, it is not enough to focus only on the bandwidth performance, but also factor in its thickness. Therefore, to highlight these RCS reducers' performance of both bandwidth and thickness, a figure of merit (FoM) is also introduced in the table. Here, it is worth noting that the FoM is a metric used to assess the comprehensive performance of the devices in a particular area, which is a

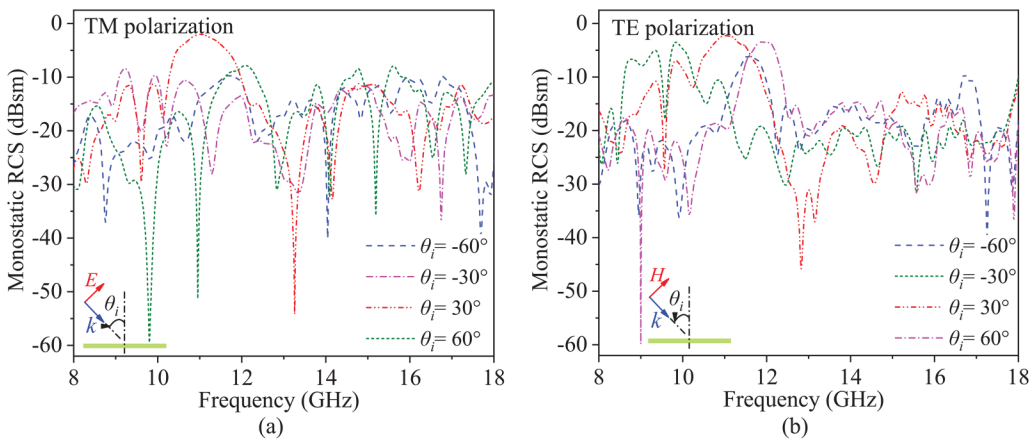

FIG. 17. The measured monostatic RCS of the designed CMS under oblique incidences for (a) TM and (b) TE polarizations.

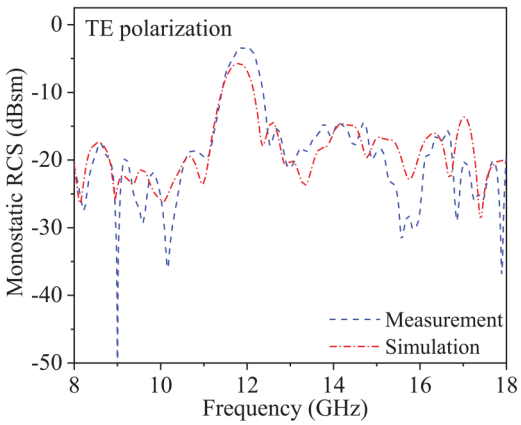

FIG. 18. The comparison diagram of the measurements and the simulations for the incident angles of ($\theta = 60°$, $\varphi = 0°$) at the TE polarization.

fused result of multiple parameters of interest. For example, in the evaluation of bistatic RCS reduction performance, the FoM is represented by the quotient obtained from dividing the maximum bistatic RCS with MS by maximum bistatic RCS without MS.[23] In this paper, the FoM is given as the ratio of FBW to the overall electrical thickness of the device, i.e.,[52]

$$\mathrm{FoM} = \frac{f_H - f_L}{(f_H + f_L)/2} \Big/ \frac{h}{\lambda_l} = \frac{C \cdot \Delta f}{f_o f_L h}, \tag{13}$$

where h is the overall thickness of the device, C is the speed of light, λ_l is the wavelength of the lowest frequency of 10 dB RCS reduction band, f_0 and f_L represent the center and lowest frequency of that, respectively, and Δf represents the absolute bandwidth. Given these definitions, the data in Table II reveal that the designed CMS is capable of accommodating both the bandwidth and thickness requirements simultaneously, while still maintaining low cost and ease of manufacturability.

V. CONCLUSION

In this paper, a cost-effective CMS based on the principle of destructive interference was designed and fabricated using the lossy FR4 material for reducing the wideband monostatic RCS of the metallic planar targets. The two AMC meta-atoms with single and dual resonances can achieve the phase deviation of 180° ± 37° over a wide frequency range. Due to the inevitable resonance losses and the quasi-periodic effect, the simulated frequency range of 10 dB RCS reduction exhibits a slightly rightward shift from that of the theoretical prediction. The simulated and measured monostatic RCS curves prove that the designed CMS can reduce the backward scattered RCS under normal incidence for more than 10 dB over the frequency range of 8.1–16 GHz, besides, owing to the frequency-dependent characteristics of the dispersion materials, the bandwidth of 10 dB RCS reduction from the measurements exceeds that of the simulations, and it is precisely for this reason that the measured bandwidth of 8 dB RCS reduction covers the entire frequency range of 8–18 GHz. In conclusion, with a good FoM, our work also provides a comprehensive examination of the AMC meta-atoms' physical mechanisms and also systematically evaluates discrepancies between simulations and predictions, as well as between simulations and experiments, which can offer a good reference for future research on the low-cost CMS design.

ACKNOWLEDGMENTS

This work was supported by the National Key Research and Development Plan of China under Grant No. 2021YFB3500403.

AUTHOR DECLARATIONS

Conflict of Interest

The authors have no conflicts to disclose.

Author Contributions

Chao Wang: Conceptualization (lead); Methodology (lead); Software (lead); Validation (lead); Writing – original draft (lead). **Ru-Zhi Wang:** Supervision (equal); Validation (equal). **Sheng-Jun Zhang:** Supervision (supporting). **Han Wang:** Data curation (equal); Software (equal). **Wen-Song Wang:** Supervision (supporting); Validation (supporting).

TABLE II. Performance comparisons of our proposed CMS with other wideband checkerboard designs.

Ref./Year	Number of layers	Thickness (mm), (λ_l)	Substrate used	10 dB RCS reduction band in GHz (FBW)		FoM	Polar.
				Simulated	Measured		
15/2019	1	2, (0.085 λ_l)	F4B	11.8–15.8 (29%)	12.8–15.7 (20.35%)	2.38	Dual
47/2023	1	0.8, (0.068λ_l)	FR4	25.8–35.3 (30.1%)	Not explicitly listed	4.52	Single
48/2019	2	12, (0.15λ_l)	RO4350B	3.78–10.08 (90.9%)	3.77–10.14 (91.6%)	6.07	Dual
49/2023	2	3.35, (0.082 λ_l)	PMMA	7.4–13.4 (57.7%)	7.4–13.4 (57.7%)	6.98	Dual
50/2019	1	3.175, (0.084 λ_l)	Taconic TLY-5	8–16 (66.7%)	8–16.32 (68.4%)	8.08	Dual
51/2020	2	9, (0.14 λ_l)	FR4	4.67–19.12 (121%)	Not explicitly listed	8.67	Single
This work	1	3, (0.08 λ_l)	FR4	8.1–16 (65.56%)	8–16.43 (69%)	8.63	Dual

DATA AVAILABILITY

The data that support the findings of this study are available from the corresponding author upon reasonable request.

REFERENCES

[1]C. A. Balanis, *Antenna Theory: Analysis and Design*, 3rd ed. (John Wiley & Sons, Inc., Hoboken, NJ, 2003).
[2]E. F. Knott, J. F. Shaeffer, and M. Tuley, *Radar Cross Section*, 2nd ed. (SciTech Publishing, Inc., Raleigh, 2004).
[3]Y. Xi, W. Jiang, K. Wei, T. Hong, T. Cheng, and S. Gong, IEEE Antennas Wirel. Propag. Lett. **21**, 656–660 (2022).
[4]Y. Fan, N.-H. Shen, F. Zhang *et al.*, ACS Photonics **5**, 1612–1618 (2018).
[5]Y. Shang, Z. Shen, and K. Feng, J. Appl. Phys. **120**, 045109 (2016).
[6]H. Wang, Z. Qin, L. Huang *et al.*, PhotoniX **3**, 10 (2022).
[7]C. Qian, B. Zheng, Y. Shen *et al.*, Nat. Photonics **14**, 383–390 (2020).
[8]S.-D. Zhao, H.-W. Dong, X.-B. Miao, Y.-S. Wang, and C. Zhang, Phys. Rev. Appl. **17**, 034019 (2022).
[9]L. Shao, W. Zhu, M. Y. Leonov, and I. D. Rukhlenko, J. Appl. Phys. **125**, 203101 (2019).
[10]Y. Wu, H. Lin, J. Xiong *et al.*, J. Appl. Phys. **129**, 134902 (2021).
[11]Z. R. Ren, H. C. Yin, X. Sun *et al.*, Opt. Mater. **131**, 112689 (2022).
[12]Y. Han, S. Gong, J. Wang, Y. Li, S. Qu, and J. Zhang, IEEE Trans. Antennas Propag. **68**, 1419–1425 (2020).
[13]X. Chen, X. Jia, Z. Wu *et al.*, IEEE Antennas Wirel. Propag. Lett. **18**, 1016–1020 (2019).
[14]H.-X. Xu, S. Ma, X. Ling *et al.*, ACS Photonics **5**, 1691–1702 (2018).
[15]W. Li, Y. Z. Zhang, T. L. Wu, J. Cao, Z. H. Chen, and J. G. Guan, Results Phys. **12**, 1964–1970 (2019).
[16]Y.-T. Zhao, J. Chen, Y. Wei *et al.*, J. Appl. Phys. **131**, 165108 (2022).
[17]A. Murugesan, D. Natarajan, and K. T. Selvan, IEEE Antennas Wirel. Propag. Lett. **20**, 493–497 (2021).
[18]A. Y. Modi, C. A. Balanis, C. R. Birtcher, and H. N. Shaman, IEEE Trans. Antennas Propag. **65**, 5406–5417 (2017).
[19]M. Paquay, J. C. Iriarte, I. Ederra, R. Gonzalo, and P. Maagt de, IEEE Trans. Antennas Propag. **55**, 3630–3638 (2007).
[20]Z. Zhou, K. Chen, J. Zhao *et al.*, Opt. Express **25**, 30241–30252 (2017).
[21]F. Costa, S. Genovesi, A. Monorchio, and G. Manara, IEEE Antennas Wirel. Propag. Lett. **13**, 27–30 (2014).
[22]M. Cos, Y. Alvarez, and F. Las-Heras, Progress Electromagn. Res **117**, 103–119 (2011).
[23]A. Edalati and K. Sarabandi, IEEE Trans. Antennas Propag. **62**, 747–754 (2014).
[24]W. Chen, C. A. Balanis, and C. R. Birtcher, IEEE Trans. Antennas Propag. **63**, 2636–2645 (2015).
[25]Q. Li, Y. Pang, Y. Li *et al.*, J. Appl. Phys. **124**, 065107 (2018).
[26]H. B. Jing, Q. Ma, G. D. Bai, L. Bao, J. Luo, and T. J. Cui, J. Appl. Phys. **124**, 023102 (2018).
[27]J. C. I. Galarregui, A. T. Pereda, J. L. M. D. Falcón, I. Ederra, R. Gonzalo, and P. D. Maagt, IEEE Trans. Antennas Propag. **61**, 6136–6143 (2013).
[28]W. Chen, C. A. Balanis, and C. R. Birtcher, IEEE Trans. Antennas Propag. **64**, 4133–4138 (2016).
[29]W. C. Li, B. H. Zhang, Y. Ying *et al.*, Opt. Mater. **133**, 112801 (2022).
[30]Y. Azizi, M. Soleimani, and S. H. Sedighy, J. Appl. Phys. **128**, 205301 (2020).
[31]Y. Zhang, R. Mittra, B. Z. Wang, and N. T. Huang, Electron. Lett. **45**, 484–485 (2009).
[32]J. Yang, Y. Li, Y. Cheng *et al.*, J. Appl. Phys. **127**, 235304 (2020).
[33]J. Su, Y. Lu, Z. Zheng *et al.*, J. Appl. Phys. **120**, 205107 (2016).
[34]L. Liu, W. Liu, and Z. Song, J. Appl. Phys. **128**, 093104 (2020).
[35]J. Su, Y. Lu, J. Liu, Y. Yang, Z. Li, and J. Song, IEEE Trans. Antennas Propag. **66**, 7091–7099 (2018).
[36]S. Sui, J. Wang, Y. Pang, J. Zhang, Z. Xu, and S. Qu, J. Phys. D: Appl. Phys. **55**, 275002 (2022).
[37]C. Tao and T. Itoh, IEEE Trans. Antennas Propag. **68**, 6193–6203 (2020).
[38]Y. Ran, L. Shi, J. Wang, Y. Ma, J. Li, and Y. Liu, J. Appl. Phys. **130**, 023106 (2021).
[39]Q. Chen, D. Sang, M. Guo, and Y. Fu, IEEE Trans. Antennas Propag. **66**, 4105–4114 (2018).
[40]E. Ameri, S. H. Esmaeli, and S. H. Sedighy, Appl. Phys. Lett. **112**, 201601 (2018).
[41]K. Kandasamy, B. Majumder, J. Mukherjee, and K. P. Ray, IEEE Antennas Wirel. Propag. Lett. **14**, 1638–1641 (2015).
[42]Y. Jing, Y. Li, J. Zhang *et al.*, J. Phys. D: Appl. Phys. **51**, 475103 (2018).
[43]W. Wang, Z. Fang, K. Tang *et al.*, IEEE Trans. Antennas Propag. **71**, 318–329 (2023).
[44]C. Wang, R. Z. Wang, Z. L. An, Y. S. Zhou, Z. X. Tang, and S. J. Zhang, J. Phys. D: Appl. Phys. **55**, 485001 (2022).
[45]J. Huang, *Antenna Analysis Techniques*, 3rd ed. (John Wiley & Sons, Inc., Hoboken, NJ, 2007).
[46]F. Yang and Y. Rahmat-Samii, *Surface Electromagnetics: With Applications in Antenna, Microwave, and Optical Engineering*, 3rd ed. (Cambridge University Press, Cambridge, 2019).
[47]M. F. El-Sewedy and M. A. Abdalla, IEEE Trans. Antennas Propag. **71**, 1988–1992 (2023).
[48]D. Sang, Q. Chen, L. Ding, M. Guo, and Y. Fu, IEEE Trans. Antennas Propag. **67**, 2604–2612 (2019).
[49]Y. D. Wang, G. Z. Wu, W. Yibo, Q. Q. Jia, and J. G. Liu, Opt. Mater. **135**, 113380 (2023).
[50]S. H. Kim and Y. J. Yoon, IEEE Antennas Wirel. Propag. Lett. **18**, 896–900 (2019).
[51]W. J. Liao, Y. C. Hou, and S. T. Chen, IEEE Trans. Antennas Propag. **68**, 2277–2289 (2020).
[52]Y. F. Fu, J. D. Ji, Y. J. Wang, F. K. Zhou, C. Wang, and P. Chen, IEEE Antennas Wirel. Propag. Lett. **21**, 878–882 (2022).